A full meshless algorithm for super-resolution in image velocimetry based on KNN-PTV and constrained RBFs

Iacopo Tirelli[1,*], Miguel Alfonso Mendez[2], Andrea Ianiro[1] and Stefano Discetti[1]

1: Department of Aerospace Engineering, Universidad Carlos III de Madrid, Avda. Universidad 30, Leganés, 28911, Madrid, Spain
2: Environmental and Applied Fluid Dynamics, von Karman Institute for Fluid Dynamics, Waterloosesteenweg 72, Sint-Genesius-Rode,1640,Bruxelles,Belgium

*Corresponding author: iacopo.tirelli@uc3m.es

Keywords: KNN, c-RBFs, meshless algorithm, PTV, PIV.

ABSTRACT

A novel full meshless super-resolution method for image velocimetry is proposed. This method builds upon the combination, presented in Tirelli et al. (2023a), of K-nearest neighbour Particle Tracking Velocimetry (Tirelli et al., 2023b, KNN-PTV) and constrained Radial Basis Functions regression (Sperotto et al., 2022, c-RBFs). The main novelty is that the algorithm is implemented here in a fully meshless version, i.e. it does not require the definition of a common Eulerian grid at any step of the process. KNN-PTV enhances the spatial resolution of vector fields by exploiting data coherence in space and time, even for non-time-resolved measurements. On the other hand, c-RBFs provide an analytical representation of the field from scattered data while allowing the introduction of physical constraints. In this new version, the dictionary to blend data from different snapshots is computed with a meshless POD approach developed by the authors and presented in another contribution to this conference. This approach removes the last constraint of Eulerian grids and paves the way for a fully meshless algorithm. The algorithm is validated on a challenging 2D synthetic case, such as turbulent channel flow, and an experimental case involving the separation bubble around the frontal portion of a Ground Transportation System (GTS).

1. Introduction

Measuring turbulent flows poses challenges due to the vast range of spatial and temporal scales involved, a range that expands with increasing Reynolds numbers. While Particle Image Velocimetry (PIV) has become a robust tool for this purpose (Westerweel et al., 2013), its ability to resolve turbulent scales is constrained by the sensor size and the interparticle spacing in images. Despite the potential to enhance spatial resolution through time resolution by exploiting consistency over short sequences (Sciacchitano et al., 2012; Schneiders et al., 2014), it appears that two-frame PIV has reached its physical limit in terms of dynamic spatial range. One way to overcome these limitations is to recognize that each vector realization is a sample from an underlying statistical

distribution. Individual vectors can be obtained with super-resolution Particle Tracking Velocimetry (Keane et al., 1995, super-resolution PTV), and are the natural output of modern 3D tracking methods (Wieneke, 2012; Schröder & Schanz, 2023). The main advantage of using individual vectors with respect to cross-correlation approaches is the reduced systematic errors. Large amounts of data from different snapshots can thus be used to improve spatial resolution and measurement accuracy.

Recent advances in data-driven and machine-learning algorithms have led to resolution-enhancement methods analyzing statistical distributions of available samples. Contributions following this path include Data-Enhanced PTV (Cortina-Fernández et al., 2021, DEPTV), KNN-PTV (Tirelli et al., 2023b), and randomly-seeded super-resolution generative adversarial networks (Güemes et al., 2022, RaSeedGAN). KNN-PTV stands out for its simplicity of implementation and its capability to deliver high-resolution vector fields and uncertainty and represents the starting point of the methodology presented in this work.

In the recent work presented by Tirelli et al. (2023a), we demonstrated the capability of recovering spatial resolution coupling KNN-PTV with the constrained regression via Radial Basis Functions (c-RBFs) introduced by Sperotto et al. (2022). The underlying hypothesis is that the principle leveraged by KNN-PTV can be applied to artificially increase the particle density of individual snapshots, offering denser scattered distributions to c-RBFs and resulting in a physically constrained super-resolution. The KNN-PTV explores an ensemble of statistically-independent snapshots to identify local similarity in terms of flow structures at various time instants. Initially, the algorithm divides the measurement domain into subdomains, aiming to ensure similarity on a local scale. Subsequently, it employs an unsupervised KNN search within the space of significant flow features, which are derived through Proper Orthogonal Decomposition (Lumley, 1967, POD) of training data obtained via cross-correlation-based methods or binning of PTV data. The method blends local vectors from snapshots that are locally similar and artificially increases the particle density, feeding the constrained regression with enriched particle fields. This allows placing smaller Gaussian basis, well supported, that can easily model the smallest scales.

The enforcement of c-RBFs provides as natural output an analytical representation of the flow field that does not depend on the mesh selection. The final limitation of this algorithm that constrained it to a structured Eulerian grid stems from the need to employ POD. The conventional POD is based on the decomposition of discrete data.

Recently, we introduced a new approach for extracting POD modes directly from particle distributions, referred to as meshless POD, that removes the need to pass through Eulerian grids. The meshless modes obtained through this new method have demonstrated increased accuracy, primarily by avoiding the modulation error associated with the interpolation process related to second-order spatial derivatives (Scarano, 2003).

In the context of this work, the integration of this methodology in the algorithm introduces two

advantages. Firstly, the features extracted are less biased by modulation errors, enabling more accurate identification of neighbours. On the other hand, this opens up the possibility of developing a fully meshless algorithm. The results can be interpolated onto the most suitable mesh, whether it is coarser for a focus on larger scales or finer in cases where smaller scales or specific coordinates (e.g., radial) are of interest. This flexibility in mesh selection enhances the adaptability of the approach to different needs and purposes.

The methodology is described in Sec. 2, while preliminary results on a Direct Numerical Simulation (DNS) of the turbulent channel flow are presented in Sec. 3.

2. Methodology

The workflow of this updated version builds upon the one described in Tirelli et al. (2023a). The main idea is that we merge particles of different snapshots to increase the spatial resolution. The merging is "activated" once local similarity is identified, i.e. the domain is divided into subregions, and for each of them at each time instants we search for the most similar realizations within the time ensemble. If the flow fields in a subdomain at different time instants are deemed to be sufficiently similar, their particles are merged and a denser snapshot is created. Similarity is assessed with a local POD. The data are then used to feed a constrained interpolator based on RBFs to obtain an analytical description of the flow field.

The main advance we propose here is to remove to need of passing through an interpolation on an Eulerian grid in any of the steps of the process. The algorithm can be summarised in 4 main steps:

1. Vector calculation via super-resolution PTV (Keane et al., 1995) or similar methods.
2. Local POD analysis to assess similarity: the domain is divided into subdomains where the POD extracts the i^{th} local space of features $\Theta_{L_i} = \Psi_{L_i}\Sigma_{L_i}$. This process is hereby carried out using a fully meshless POD formulation, summarized below. This will be the feature set that drives the KNN search for neighbours.
3. Identification of the optimal number of neighbours as the value that explains the 90% of the variance of the reduced temporal correlation matrix K_r.
4. Velocity field reconstruction using the c-RBFs as described in Sperotto et al. (2022) on the enriched particle distribution obtained following the map of neighbours of the previous step.

The most notable innovation of this new version is the introduction of the recently proposed meshless POD as a tool for feature extraction in step 2. This eliminates the need to build low-resolution fields for training using binning, as in Tirelli et al. (2023b). The fields for local POD are replaced by

approximations of analytical functions describing the velocity fields at specific time instants obtained directly from the particle distributions. This approximation $\tilde{u}(\mathbf{x}, t_i)$ is achieved employing c-RBFs:

$$\tilde{u}(\mathbf{x}, t_i) = \sum_{q=1}^{N_b} w_q(t_i)\gamma_q(\mathbf{x}), \tag{1}$$

where N_b is the number of basis functions used in the approximation (in this case it coincides with the number of particles N_p), γ_q is the q^{th} regression basis, and w are the corresponding weights. The vector $\mathbf{x}$ contains the coordinates on which the data are evaluated at the i^{th} time instant t_i among the total N_t time instances. With no loss of generality, the basis functions employed in this work are thin-plate RBFs.

Furthermore, the POD is now carried out directly on the analytical representations of the fluctuating velocity fields, again avoiding the step of interpolating on an Eulerian grid and the associated modulation error (Tirelli et al., 2023c). The inner product in the spatial domain among all the velocity field approximations allows us to compute the temporal correlation matrix $\mathbf{K}$ through the definition of the inner product in the continuous domain, whose generic element K_{ij} is given by:

$$K_{ij} = \frac{1}{\parallel \Omega \parallel} \int_{\Omega} \tilde{u}(\mathbf{x}, t_i)\ \tilde{u}(\mathbf{x}, t_j)\ d\Omega. \tag{2}$$

with Ω is the spatial domain considered.

The temporal modes and eigenvalues needed to build the feature dataset Θ_{L_i} are then obtained by decomposing $\mathbf{K}$ via eigenvalue decomposition. This step is performed for each subdomain considering only the particles that fall in the i^{th} subdomain. This meshless approach results in a more precise decomposition, leading to enhanced accuracy in feature extraction and, consequently, improved identification of neighbours.

The third step is the evaluation of the optimal number of neighbours. It is extracted directly from the temporal correlation matrix of the specific subdomain. First of all, the rank r is computed as:

$$r = argmin \left(\frac{\sum_{j=1}^{i} diff(\sigma_j)}{\sum_{j=1}^{N_t} diff(\sigma_j)} > 0.9 \right). \tag{3}$$

This approach allows us to determine the minimum number of modes that explain 90% of the variance, highlighting their significance. Utilizing this value, a reduced-order version of the correlation matrix K_r is computed, incorporating only the first r modes.

It is essential to emphasize that this step exclusively yields the count of neighbours without specifying their positions. The positions are determined by the KNN leveraging the more refined fea-

ture space. Enhanced precision is achieved by using the mesh-free modes. This process is applied independently for each of the local subdomains in order to achieve a map of neighbours.

The high-resolution flow fields are achieved through c-RBFs regression as explained in Tirelli et al. (2023a). Bearing in mind the definition of $\tilde{u}$ in Eq. 1, for this specific case only Gaussian basis has been employed, while in the previous version there was also a polynomial set. Despite the well-known significant role that such a basis plays in terms of regularization of the regression and approximation of global behaviour, it is also acknowledged that its effectiveness heavily relies on the user's expertise. This is crucial as the correct scaling of the domain is required to position them optimally. Inspired by the concept of the first KNN-PTV, aiming for an end-to-end tool that starts from raw images and yields output with minimal user intervention, the polynomial function has been excluded. This decision, while sacrificing a degree of accuracy, reduces the number of parameters to be selected. Future investigations will focus on identifying a set of bases that strikes the best compromise between accuracy and simplicity.

3. Validation and preliminary results

3.1. Turbulent channel flow

The algorithm proposed was tested using synthetic PTV data derived from a direct numerical simulation (DNS) of a turbulent channel flow obtained from the Johns Hopkins Turbulence Database (`http://turbulence.pha.jhu.edu/`). The dimensions of the channel consist of 2 half-channel-heights h from wall to wall, $3\pi h$ in the span-wise direction and $8\pi h$ in the streamwise direction. For all simulation settings, please refer to Li et al. (2008). In this simulated experiment, subdomains of $2h \times h$ are extracted in the streamwise and wall-normal directions, respectively. The resolution is set at 512 pixels$/h$ and the particle image density is 0.01 particles per pixel. To reduce the correlation between different samples, the snapshots are generated with a time separation of 1 convective time. A large number of snapshots are extracted by exploiting flow homogeneity in the streamwise and spanwise directions. The subdomains are separated by $2h$ in the streamwise and $0.25h$ in the spanwise direction, resulting in a total of $N_t = 11856$ generated snapshots. The performance of the algorithm was evaluated using the normalized root mean square error δ_{RMS}:

$$\delta_{RMS} = \frac{\sqrt{\frac{\sum_{i=1}^{N_t}(U_i - U_{DNS_i})^2 + (V_i - V_{DNS_i})^2}{N_t}}}{U_b}, \tag{4}$$

with U_b as bulk velocity, equal to 7.5 pixels, and U_{DNS}, V_{DNS} indicate respectively the streamwise and wall-normal velocity components of the reference velocity field.

A qualitative comparison among the methods on an instantaneous streamwise velocity field con-

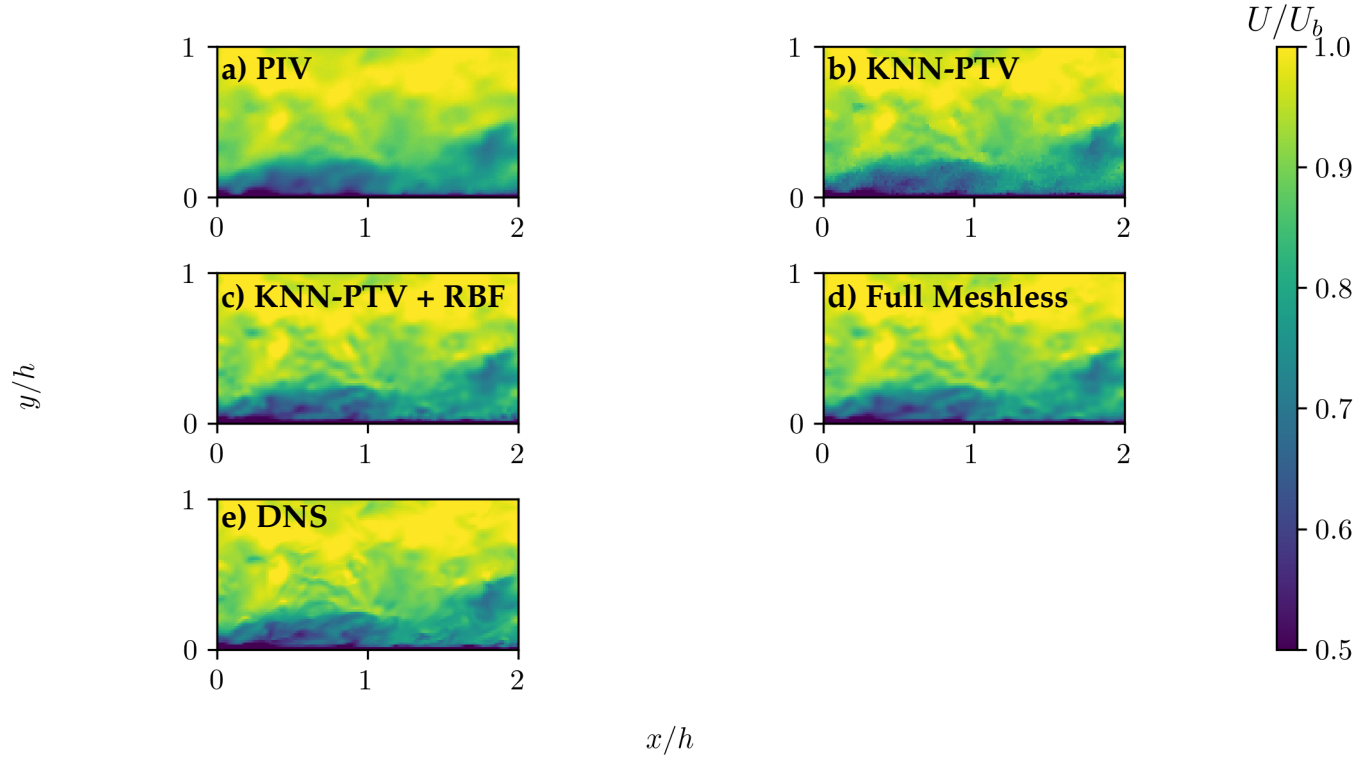

Figure 1. Instantaneous streamwise velocity field contours estimated with: (a) standard PIV with interrogation window of 32×32 pixels, (b) KNN-PTV, (c) KNN-PTV + RBF. The reference field from the original DNS is included for comparison (d) .

PIV IW = 32	KNN-PTV	KNN-PTV + RBF	Full meshless
0.0222	0.0196	0.0173	0.0170

Table 1. Spatial average of the root mean square error $\langle \delta_{RMS} \rangle$ evaluated for PIV with interrogation window of 32 pixels, KNN-PTV, KNN-PTV with the help of RBF and the full meshless version of the algorithm

tours is proposed Fig.1. The reference is standard PIV with an interrogation window of 48 pixels, simulated by filtering the data with a moving average and down-sampling the result. The bias error on the mean flow has been corrected according to Tirelli et al. (2023c). This represented the benchmark for the first version of KNN-PTV, which exploiting local similarity in the datasets was able to recover spatial resolution, especially in the near-wall region, dominated by the smallest scales filtered out by the moving average process of PIV. A significant improvement is evident when comparing this contour with the version of the algorithm proposed by Tirelli et al. (2023a). Here the weighted average system used for reconstructing the high-resolution field in the first algorithm has been substituted with a more robust constrained regression based on radial basis functions. The enhancement in spatial resolution is substantial. Additionally, a key innovation introduced by this version is the analytical approximation of the flow field as output. On the other hand, the full meshless version proposed here removes the last constraints imposed by Eulerian

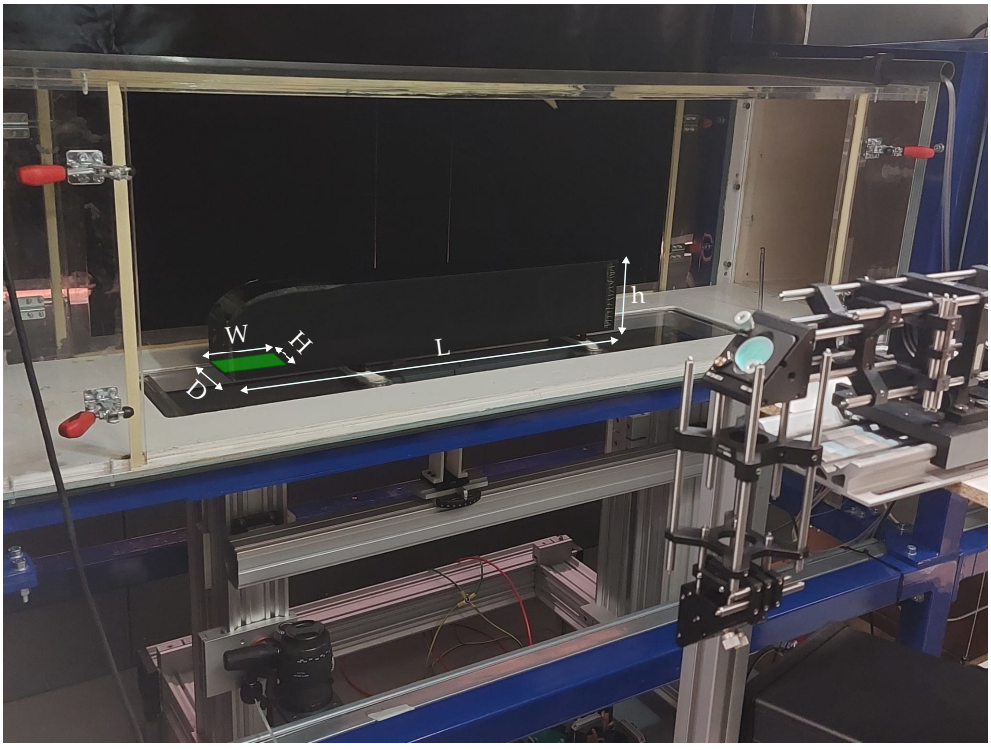

Figure 2. Picture of the experimental setup

grids. The spatially-averaged root mean square error $\langle \delta_{RMS} \rangle$ is reported in Table 1.

For this specific application, the c-RBFs regression was constrained to have no-slip conditions at the wall. Additionally, divergence-free condition has been applied only as a penalty to regularize the regression. The domain contained about 2500 collocation points following the clustering approach explained in Sperotto et al. (2022).

It is worth noting that while all the previous methodologies have likely already reached their peak performance, the results of the full meshless algorithm are merely preliminary and have not undergone any specific tuning. This is an encouraging outcome, suggesting the potential for further investment in the development of this full meshless algorithm.

3.2. Separation bubble

The experimental test case involves the investigation of the separation bubble around the head of a scale-model Ground Transportation System (GTS) without wheels (width $D = 85$ mm, height $h = 120$ mm and length $L = 650$ mm). The truck naturally presents a separation bubble when facing the flow. For this reason, the region of interest is restricted to the upstream region, spanning a domain with height $H = 38$ mm and width $W = 139$ mm. The experiment was carried out in the Göttingen-type wind tunnel of the Department of Aerospace Engineering at Universidad Carlos

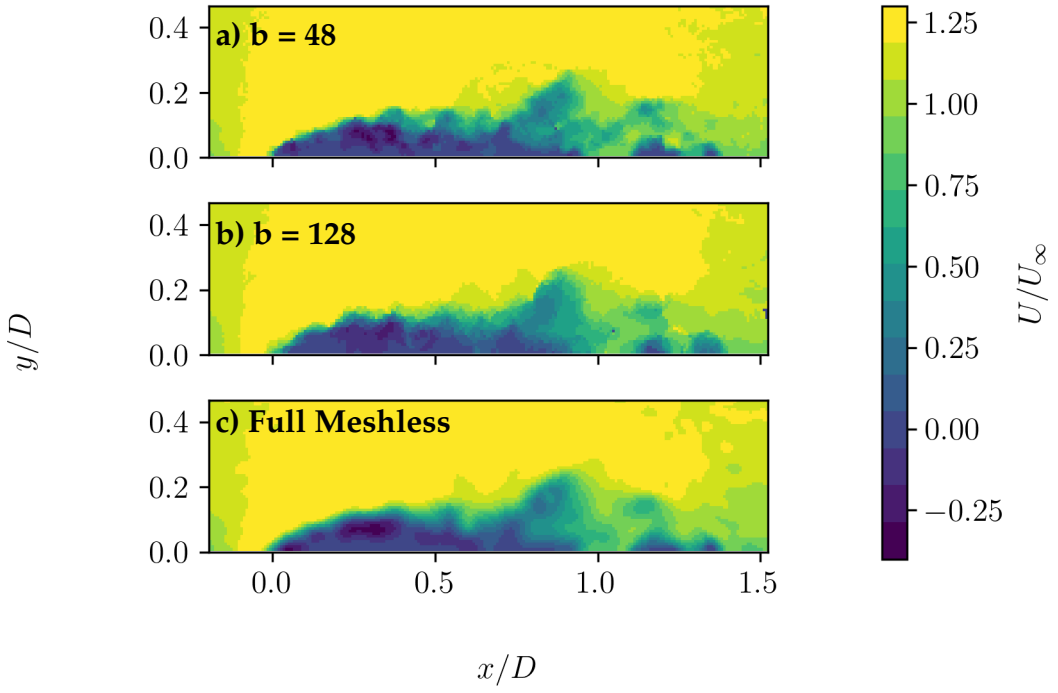

Figure 3. Instantaneous streamwise velocity field contours estimated with: (a) moving average $b = 48$ pixels, (b) moving average $b = 128$ pixels and (c) full meshless.

III de Madrid.

The experimental setup is reported in Fig 2. Illumination is provided by a cavity Ng:YAG Quantel Evergreen laser. The flow is seeded with droplets of Di-Rthyl-Hexyl-Sebacate (DEHS) with $1\ \mu m$ diameter generated by a Laskin nozzle. The PIV images (2560×700 pixels) were recorded with an Andor Zyla sCMOS 5.5 MP, with a resolution of 18.4 pix/mm. A Quantum composer 9520 Series Pulse Delay Generator has been employed to coordinate illumination and recording. Other details about the experimental setup are reported in Tab 2.

Velocity vectors are obtained using a super-resolution Particle Tracking Velocimetry (PTV) method (Keane et al., 1995). A multi-step image deformation algorithm (Scarano, 2001), utilizing high-accuracy interpolation schemes (Astarita & Cardone, 2005; Astarita, 2007), is employed to determine the predictor for the biased search. Others details about the post processing are summarised in the last row of Tab. 2.

The PTV analysis yields an average of 15000 vectors per snapshot, which corresponds to 0.008 vectors per pixel. For this experimental test case the main difficulties are related to the lack of an appropriate ground truth to be used as a reference. To overcome this problem, we derive the ground truth from a moving average with a bin size $b = 48$ pixels on this vector distribution. Vectors are then randomly eliminated from the dataset, reducing their number to 1500 and thereby decreasing the density by a factor of 10. This results in an average of 10 particles per 128×128

Table 2. Experimental setup details.

Flow facility	Göttingen-type wind tunnel. Test section: 0.4 m $\times$ 0.4 m $\times 1.5$ m. Velocity range: 4 m/s to 20 m/s. Turbulence intensity below 1%.
Seeding	Laskin nozzle. Droplets of Di-Ethyl-Hexyl-Sebacate (DEHS) with $d = 1\,\mu$m.
Illumination	Dual cavity Ng:YAG Quantel Evergreen laser 200 mJ/pulse at 10 Hz.
Imaging	Andor Zyla sCMOS 5.5 MP (2560×2160) pixel array, 6.5×6.5 μm pixel size, resolution 18.4 pix/m. Objective Tokina 100 mm lens. $f/\# = 16$.
Post-processing	POD background removal (Mendez et al., 2017), iterative multi-grid/multi-pass algorithms (Willert & Gharib, 1991; Soria, 1996), image deformation (Scarano, 2001), B-spline interpolation (Astarita & Cardone, 2005; Astarita, 2007).

pixel bin. This downsampled vector distribution is employed to perform the proposed algorithm and a moving average with $b = 128$ pixel, used for comparison. A total of 4000 snapshots are used for this analysis.

The preliminary results are compared in Fig. 3. The spatial coordinates are normalized using the height of the truck D, while the velocities are normalized using the freestream velocity $U_\infty = 10$ m/s. For the full meshless KNN-PTV approach, a total of 4251 collocation points are placed in the domain, with the no-slip condition enforced as constraints near the sides of the truck. From a qualitative comparison, the reconstruction produced by the proposed algorithm appears to be smoother if compared to the case with $b = 128$ pixels. This effect is likely due to the Gaussian basis, which tends to regularize the data. Overall, the method demonstrates good accuracy in capturing the velocity peaks that are filtered out by the moving average process, especially around the head of the bubble. The same metric reported in Eq. 4 is used to assess the accuracy of the methodologies. The values of δ_{RMS} are very close: 0.097 for the full meshless algorithm versus 0.106 for the binned one. The algorithm thus shows significant potential for improvement, especially considering that these preliminary results were obtained without any tuning. Additionally, other combinations of basis functions and strategies for evaluating similarity could be explored in future work.

4. Conclusions

A novel meshless super-resolution technique has been proposed for image velocimetry, leveraging the combined strengths of KNN-PTV and c-RBFs. This method enhances particle density by "borrowing" particles from analogous snapshots, even in the absence of time resolution, and strengthens regression robustness through the integration of physical constraints, all in a fully meshless

manner. Preliminary results demonstrate promising outcomes in terms of reconstruction accuracy and spatial resolution, validated through benchmark analyses on a synthetic fully-turbulent flow test case and the experimental case of a separation bubble. Moreover, this approach is mesh-independent and provides analytical representations of flow fields that are easy to interpolate and differentiate on any grid, paving the way for the extraction of high-resolution turbulent statistics. This adaptability to the specific needs and purposes of the investigation represents an important novelty. The methodology is anticipated to be particularly advantageous for 3D flow analysis, where the need for spatial resolution is more urgent than planar application. Furthermore, the use of constrained regression can compensate for the larger interparticle spacing of these cases enforcing constraints that include the physics behaviour of the flow. The authors are currently extending this methodology to 3D measurements.

Acknowledgment

This project has received funding from the European Research Council (ERC) under the European Union's Horizon 2020 research and innovation program (grant agreement No 949085). However, the views and opinions expressed are those of the authors only and do not necessarily reflect those of the European Union or the European Research Council. Neither the European Union nor the granting authority can be held responsible for them.

The GTS experiment presented herein was designed by Mr. Lucas Schneeberger. We kindly thank him for granting the availability of the experimental setup to collect the dataset for the experimental validation of our method.

References

Astarita, T. (2007). Analysis of weighting windows for image deformation methods in PIV. *Experiments in fluids*, *43*, 859–872.

Astarita, T., & Cardone, G. (2005). Analysis of interpolation schemes for image deformation methods in PIV. *Experiments in fluids*, *38*, 233–243.

Cortina-Fernández, J., Sanmiguel Vila, C., Ianiro, A., & Discetti, S. (2021). From sparse data to high-resolution fields: ensemble particle modes as a basis for high-resolution flow characterization. *Experimental Thermal and Fluid Science*, *120*, 110178.

Güemes, A., Sanmiguel Vila, C., & Discetti, S. (2022). Super-resolution generative adversarial networks of randomly-seeded fields. *Nature Machine Intelligence*, 1–9.

Keane, R., Adrian, R., & Zhang, Y. (1995). Super-resolution particle imaging velocimetry. *Measurement Science and Technology*, *6*(6), 754.

Li, Y., Perlman, E., Wan, M., Yang, Y., Meneveau, C., Burns, R., ... Eyink, G. (2008). A public turbulence database cluster and applications to study lagrangian evolution of velocity increments in turbulence. *Journal of Turbulence*(9), N31.

Lumley, J. L. (1967). The structure of inhomogeneous turbulent flows. *Atmospheric turbulence and radio wave propagation*, 166–178.

Mendez, M. A., Raiola, M., Masullo, A., Discetti, S., Ianiro, A., Theunissen, R., & Buchlin, J.-M. (2017). POD-based background removal for particle image velocimetry. *Experimental Thermal and Fluid Science*, *80*, 181–192.

Scarano, F. (2001). Iterative image deformation methods in PIV. *Measurement science and technology*, *13*(1), R1.

Scarano, F. (2003). Theory of non-isotropic spatial resolution in PIV. *Experiments in Fluids*, *35*, 268–277.

Schneiders, J. F., Dwight, R. P., & Scarano, F. (2014). Time-supersampling of 3D-PIV measurements with vortex-in-cell simulation. *Experiments in Fluids*, *55*, 1–15.

Schröder, A., & Schanz, D. (2023). 3D Lagrangian Particle Tracking in Fluid Mechanics. *Annual Review of Fluid Mechanics*, *55*.

Sciacchitano, A., Scarano, F., & Wieneke, B. (2012). Multi-frame pyramid correlation for time-resolved PIV. *Experiments in fluids*, *53*, 1087–1105.

Soria, J. (1996). An investigation of the near wake of a circular cylinder using a video-based digital cross-correlation particle image velocimetry technique. *Experimental Thermal and Fluid Science*, *12*(2), 221–233.

Sperotto, P., Pieraccini, S., & Mendez, M. A. (2022). A meshless method to compute pressure fields from image velocimetry. *Measurement Science and Technology*, *33*(9), 094005.

Tirelli, I., Ianiro, A., & Discetti, S. (2023b). An end-to-end KNN-based PTV approach for high-resolution measurements and uncertainty quantification. *Experimental Thermal and Fluid Science*, *140*, 110756.

Tirelli, I., Ianiro, A., & Discetti, S. (2023c). A simple trick to improve the accuracy of PIV/PTV data. *Experimental Thermal and Fluid Science*, *145*, 110872.

Tirelli, I., Mendez, M., Ianiro, A., & Discetti, S. (2023a). A combination of KNN-PTV and physics-constrained RBFs for super-resolution in image velocimetry. In *15th international symposium on particle image velocimetry.*

Westerweel, J., Elsinga, G. E., & Adrian, R. J. (2013). Particle image velocimetry for complex and turbulent flows. *Annual Review of Fluid Mechanics*, *45*, 409–436.

Wieneke, B. (2012). Iterative reconstruction of volumetric particle distribution. *Measurement Science and Technology*, *24*(2), 024008.

Willert, C. E., & Gharib, M. (1991). Digital particle image velocimetry. *Experiments in fluids*, *10*(4), 181–193.